MDPI

Article

Universal Virtual Synchronous Generator Based on Extended Virtual Inertia to Enhance Power and Frequency Response

Hao Liu [ID], Bo Yang, Song Xu, Mingjian Du and Shuai Lu *

School of Electrical Engineering, Chongqing University, Chongqing 400044, China
* Correspondence: shuai.lu@cqu.edu.cn

Abstract: Virtual synchronous generators (VSG) are considered a new generation of grid-friendly inverters with the same inertial support characteristics as synchronous generators (SG). However, the inertia support comes with the side effects of power and frequency response deterioration. The existing VSG power oscillation suppression methods have limitations such as complex controller parameter tuning, altering the frequency support characteristics, and power quality degradation. To address these issues, this paper proposes a universal VSG control strategy based on extended virtual inertia (VSG-EVI). Herein, the virtual inertia is no longer a constant or varying number; it is endowed with frequency domain characteristics to improve the VSG transient responses. Moreover, a detailed parameter design process is given in detail. Compared with the conventional VSG (CVSG), VSG-EVI significantly suppress the power and frequency oscillations. Compared with the existing VSG oscillation suppression methods, VSG-EVI addresses the issues of the reduction of frequency support capability, whereas the controller parametric design process is simplified with the proposed intuitive extended virtual inertia. Finally, the proposed VSG-EVI method is thoroughly validated by experiments under both grid-connected and stand-alone modes.

Keywords: virtual synchronous generator; virtual inertia; power control; power oscillation

1. Introduction

In recent years, in order to solve environmental problems and the energy crisis, fossil fuels have increasingly been replaced by renewable energy generations. Multi-energy systems are a very popular option in this transition [1–5]. Among the renewable energy sources, photovoltaic and wind power can be regarded as the most promising candidates. However, these energy sources are characterized by wide geographical distribution and intermittent power generation, and it is not easy to meet the power demand with a single type of renewable source. Therefore, microgrids integrating multiple distributed energy sources have been a focus area for research [6–9].

Inverters serve as the interaction interface from DGs to grid and load; hence, the control strategy of inverters is crucial for the safe, stable, and efficient operation of power systems and microgrids [10]. At present, inverters are mainly divided into current-controlled inverters and voltage-controlled inverters. Current-controlled inverters deliver power by injecting high-quality current into power grid, but they can only work in grid-connected (GC) mode, owing to the lack of grid-forming capability [11,12]. Voltage-controlled inverters have the ability to support both frequency and voltage, allowing DGs to operate in both GC and stand-alone (SA) modes. Compared with current-controlled inverters, voltage-controlled inverters have a wider range of application scenarios.

As for the control strategy of voltage-controlled inverters, droop control was first proposed for uninterruptible power supply (UPS) systems. Droop control can provide DGs with grid forming capability, power sharing capability, and the ability to participate in grid regulation, but it cannot provide inertial support for power systems [13,14]. As the penetration of DGs in the power system increases, the overall inertia of the power

system decreases. The lack of inertia can lead to sudden frequency changes and frequency oscillations, which is not conducive to frequency dynamic stability.

To solve the inertia reduction caused by DGs, the control strategy of the inverter interfacing energy storage devices can be modified to provide inertia response [14–16]. The main control strategies include fast frequency-power response, grid following control, virtual synchronizer control, etc. The candidates of energy storage for inertia response include pumped hydro, compressed air, superconducting magnetic, fuel cell, capacitor, ultracapacitor, flywheel, and battery. Among these energy storage options, battery storage systems (BESS) are the most popular one [17–19]. On the other hand, inertia response can be divided into current source type and voltage source type, according to the response characteristic and control method. Current source virtual inertia control is to introduce the system frequency change rate into the active power controller of the inverter, change the active power reference value, and provide active power proportional to the frequency change rate to the grid. The current source virtual inertia is essentially different from the rotational inertia of synchronous generators (SG), since it does not have the characteristic of instant sharing of the disturbance power and there is a time delay in this process. The virtual inertia of voltage source type is mainly a virtual synchronous generator (VSG): The VSG introduces the rotor motion and electromagnetic transient equation of SG in the controller of the inverter [20–23], giving the inverter the same external characteristics as SG. Since VSG has the same instant power sharing as SG, in the event of power disturbance, the energy storage can instantly absorb or release energy in response to the power deviation and maintain the power balance. Therefore, VSG can provide inertia support power without delay in the moment of power disturbance.

As the instantaneous VSG power output requires the power response of the BESS, the charge/discharge rate of the BESS needs to match the capacity of the VSG. In the long-time scale, the capacity degradation also needs to be considered. Therefore, the optimal sizing of a BESS is also a focus area for research, such as the frequency regulation of an isolated power system using a dynamic simulator of load frequency control [24] and BESS participating in the primary control reserve market with two-level profit-maximizing planning [25]. Some studies have also addressed the optimal sizing of BESSs for transmission and distribution networks [24,26].

Since VSG imitates SG, it provides the inertial support, but it also inherits the SG side effect of power and frequency oscillations. Since the transient overcurrent capability of the power electronics is much lower than that of SG, the transient characteristics of VSG must be improved to suppress power and frequency oscillations. The existing schemes to improve the transient characteristics of VSG are mainly divided into four categories. Category-1 is a parameter configuration. By adjusting the virtual inertia and droop coefficient, VSG operates in a critical damping state which contributes to the reduction of transient power overshoot and oscillation in GC mode [27]. However, the droop coefficient is limited by the maximum frequency deviation and the virtual inertia is limited by the maximum rate of change of frequency (ROCOF), making it difficult to guarantee that the VSG operates in a critical damping state in most cases. Category-2 is an adaptive dynamic parameter. In [28], alternating virtual inertia is proposed to suppress active power overshoot. In [29,30], an adaptively tuned virtual inertia and droop coefficient scheme is used to enhance frequency stability and improve power response transient characteristics. However, the dynamic virtual inertia alters the frequency support characteristics. In addition, the nonlinear control in the above scheme is potentially uncertain and the design process is somewhat complex. Category-3 is virtual-impedance-based [31,32]. However, with harmonics in the output current, the extra virtual impedance tends to amplify the output voltage distortion. Category-4 is changing the control structure of the conventional VSG (CVSG). In [33], an inertial droop control strategy is proposed, based on comparing droop control and VSG. In [34], an improved virtual inertia strategy based on differential compensation is proposed. In [35], power oscillation is suppressed by the power error feedforward. However, unlike other VSG controls, where all parameters have the same physical meaning as SG, the

schemes of Category-4 do not have parameters with clear physical meaning, making the parameter tuning process more complicated. Trial and error are often used to tune the parameters for Category-4 schemes.

To summarize the existing VSG power oscillation suppression methods, they have limitations such as complex controller parameter tuning, altering the frequency support characteristics, and power quality degradation. To address these issues, this paper further proposes a universal VSG control strategy based on extended virtual inertia (VSG-EVI). Herein, the virtual inertia is no longer a number (constant or varying); it is endowed with frequency domain characteristics to improve the VSG transient responses.

Compared with the CVSG, the proposed VSG-EVI significantly improves the power transient response characteristics, just like the existing methods of VSG oscillation suppression. Compared with the existing methods of VSG oscillation suppression, the proposed method addresses the issue of the reduction of frequency support capability, and the controller parametric design process is simplified with the proposed intuitive extended virtual inertia.

The key contributions of this paper are summarized as:

1. Established a small-signal model of the VSG system that reflects the coupling between the VSG active and reactive power loops, which is more detailed than the existing studies.
2. Proposed a universal VSG control strategy based on extended virtual inertia (VSG-EVI). Compared with the existing methods of VSG oscillation suppression, the proposed method addresses the issue of the reduction of frequency support capability.
3. The controller parametric design process is also very much simplified with the proposed intuitive extended virtual inertia, and comprehensive design constraints and a design flow considering both GC and SA modes are introduced.
4. The proposed method is thoroughly validated by experiments, showing a significant improvement of the VSG power oscillation suppression in GC mode and the frequency stability in SA mode.

The rest of the paper is organized as follows. In Section 2, the system topology and accurate small signal model of CVSG are introduced. In Section 3, VSG-EVI is proposed. In Section 4, a parameter design flow is given. Experimental results are presented in Section 5. Finally, conclusions are presented in Section 6. The nomenclature of all the symbols used in this work is listed in Nomenclature.

2. Small Signal Model of VSG

Figure 1 shows the basic structure block diagram and control strategy block diagram of CVSG. DGs are connected to the point of common coupling (PCC) via a three-phase voltage source inverter. The three-phase voltage source inverter uses an LCL-type filter, where L_1 is the inverter-side filter inductor, C is the filter capacitor, and L_2 is the inverter output inductor. L_{line} and R_{line} are the network-side line inductance and line resistance from PCC to grid, respectively. The control strategy mainly consists of the power control outer loop, virtual impedance loop, and voltage-current inner loop.

By simulating the rotor equation of SG [23], the core control equation of CVSG can be written as follows:

$$P_{set} - P_{out} = J \cdot \omega_m \cdot \frac{d\omega_m}{dt} + D \cdot \left(\omega_m - \omega_{ref} \right) \qquad (1)$$

where J is the virtual inertia; D is the damping coefficient; P_{set} and P_{out} are the command and output active power, respectively; and ω_m and ω_{ref} are the VSG output angular frequency and reference angular frequency, respectively.

In order to improve voltage stability, CVSG simulates the excitation regulator of SG by controlling the excitation current in a closed loop and regulating the internal potential to maintain a constant voltage [23]. Therefore, the reference output voltage is drooped

according to the reactive power and the controller uses an integral controller, and then the CVSG reactive loop control equation can be obtained as follows:

$$U_{ref} = \frac{1}{K \cdot s} \left[D_q \cdot (U_n - U_{out}) + (Q_{set} - Q_{out}) \right] \tag{2}$$
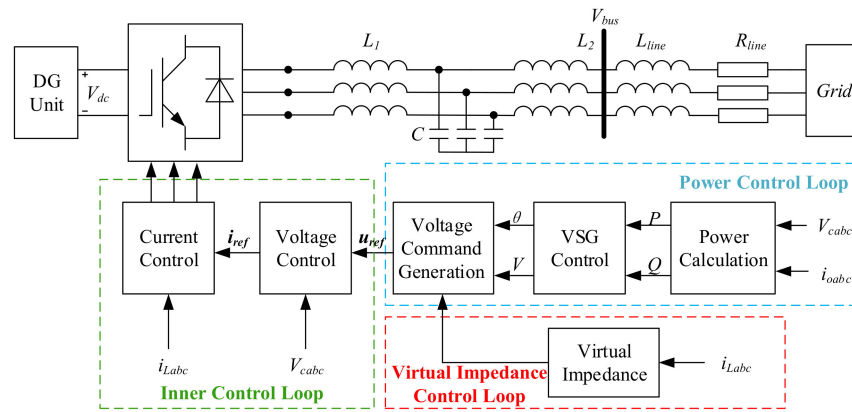
Figure 1. VSG system block diagram.

2.1. Accurate Small Signal Model of CVSG

In order to analyze the dynamic performance of VSG, it is necessary to build an accurate small signal model of VSG.

Figure 2 shows the equivalent power transmission model of CVSG. To simplify the model, L_g is used to represent the total equivalent line inductance and R_g is used to represent the total equivalent line resistance. Then, the power transfer model of CVSG is as follows:

$$L_g \frac{di_{abc}}{dt} = u_{oabc} - u_{gabc} - i_{abc} R_g \tag{3}$$
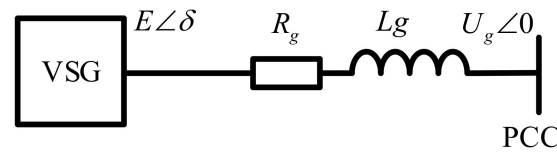
Figure 2. Equivalent power transmission model.

To facilitate analysis, Equation (3) is converted to the *dq* synchronous rotation axes as follows:

$$\begin{cases} L_g \frac{di_d}{dt} = u_{od} - u_{gd} - i_d R_g + X_g i_q \\ L_g \frac{di_q}{dt} = u_{oq} - u_{gq} - i_q R_g - X_g i_d \end{cases} \tag{4}$$

where:

$$\begin{cases} X_g = \omega_0 L_g \\ u_{gd} = U_g, u_{gq} = 0 \\ u_{od} = E \cos \delta \approx E, u_{oq} = E \sin \delta \approx E\delta \end{cases} \tag{5}$$

According to Laplace transformation, Equation (5) becomes:

$$\begin{cases} i_d = \frac{(R_g + s \cdot L_g) \cdot (E - U_g) + X_g \cdot E \cdot \delta}{X_g^2 + (s \cdot L_g + R_g)^2} \\ i_q = \frac{(R_g + s \cdot L_g) \cdot E \cdot \delta - X_g \cdot (E - U_g)}{X_g^2 + (s \cdot L_g + R_g)^2} \end{cases} \tag{6}$$

Taking the grid voltage as the reference, the inverter output capacitance voltage *E*, the grid voltage amplitude U_g, and the power angle δ, are considered to have small signal

perturbations. The small-signal model of the CVSG power transfer model can be obtained by combining Equations (5) and (6), and the instantaneous power theory as follows:

$$\begin{cases} \Delta P = G_{\delta 2P}\cdot\Delta\delta + G_{E2P}\cdot\Delta E + G_{U2P}\cdot\Delta U_g \\ \Delta Q = G_{\delta 2Q}\cdot\Delta\delta + G_{E2Q}\cdot\Delta E + G_{U2Q}\cdot\Delta U_g \end{cases} \tag{7}$$

where $G_{\delta 2P}$, G_{E2P}, G_{U2P}, $G_{\delta 2Q}$, G_{E2Q} and G_{U2Q} are shown in Equation (8):

$$\begin{cases} G_1 = X_g^2 + \left(R_g + sL_g\right)^2 \\ G_{\delta 2P} = 3\left(2E^2R_g\delta + E^2X_g\delta + EU_gX_g + 2E^2L_g\delta s\right)/G_1 \\ G_{E2P} = 3\left(2ER_g - R_gU_g + 2ER_g\delta^2 + EX_g\delta + U_gX_g\delta + s\left(2EL_g\delta^2 + 2EL_g - L_gU_g\right)\right)/G_1 \\ G_{U2P} = -3\left(E\cdot\left(R_g + sL_g\right)\right)/G_1 \\ G_{\delta 2Q} = -3\left(E^2X_g - 2E^2X_g\delta + ER_gU_g + sEL_gU_g\right)/G_1 \\ G_{E2Q} = -3\left(U_gX_g - EX_g - 2EX_g\delta + R_gU_g\delta + sL_gU_g\delta\right)/G_1 \\ G_{U2Q} = -3\left(E\delta\cdot\left(R_g + sL_g\right)\right)/G_1 \end{cases} \tag{8}$$

Combining Equations (1) and (2), we can derive the small-signal model of the VSG controller as:

$$\begin{cases} \Delta\delta = \dfrac{\Delta\omega_m - \Delta\omega_g}{s} \\ \Delta\omega_m = \dfrac{\Delta P_{set} - \Delta P_{out}}{J\omega_0 s + D} \\ \Delta E = \dfrac{\Delta Q_{set} - \Delta Q_{out}}{Ks + D_q} \end{cases} \tag{9}$$

Combining Equations (7) and (9), we can get the accurate small-signal model of the CVSG, as seen in Figure 3.
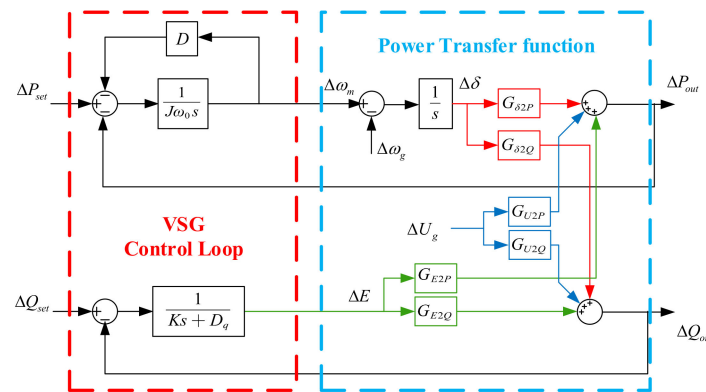
Figure 3. Accurate small-signal model of VSG.

With the detailed small-signal model derived above, the VSG system is analyzed in detail under both GC and SA modes.

2.2. GC Mode

According to Figure 3, the equivalent control block diagram of the active power control loop in GC mode can be obtained as follows Figure 4.
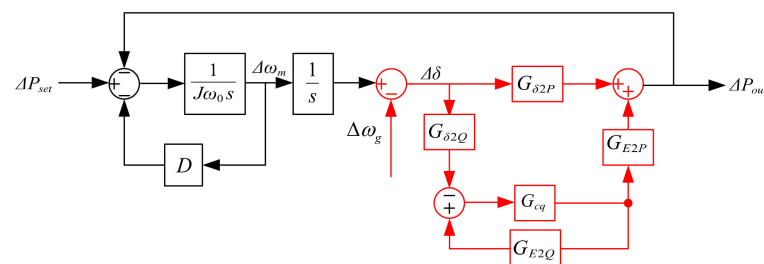
Figure 4. Active power control loop control block diagram of CVSG.

The loop gain of the CVSG active power control loop can be obtained as follows:

$$G_{OP} = \frac{G_{cp}}{s} \cdot \left(G_{\delta 2P} - \frac{G_{cq} \cdot G_{\delta 2Q} \cdot G_{E2P}}{1 - G_{cq} \cdot G_{E2Q}} \right) \tag{10}$$

where:

$$\begin{cases} G_{cp} = \frac{1}{J\omega_0 \cdot s + D} \\ G_{cq} = \frac{1}{K \cdot s + D_q} \end{cases} \tag{11}$$

The closed-loop transfer function from P_{set} to P_{out} and from P_{set} to ω_m in GC mode can be obtained as follows:

$$\left. \frac{\Delta P_{out}}{\Delta P_{set}} \right|_{GC} = \frac{G_{OP}}{1 + G_{OP}} \tag{12}$$

$$\left. \frac{\Delta \omega_m}{\Delta P_{set}} \right|_{GC} = \frac{G_{cp}}{1 + G_{OP}} \tag{13}$$

According to Equations (12) and (13), they have the same denominator; thus, we can draw the trend of pole change in GC mode, as shown below.

From Figure 5, we can see that as *J* increases, the poles of the system move closer to the imaginary axis and the system is less damped. As *D* increases, the poles of the system move closer to the real axis and the system is more damped.
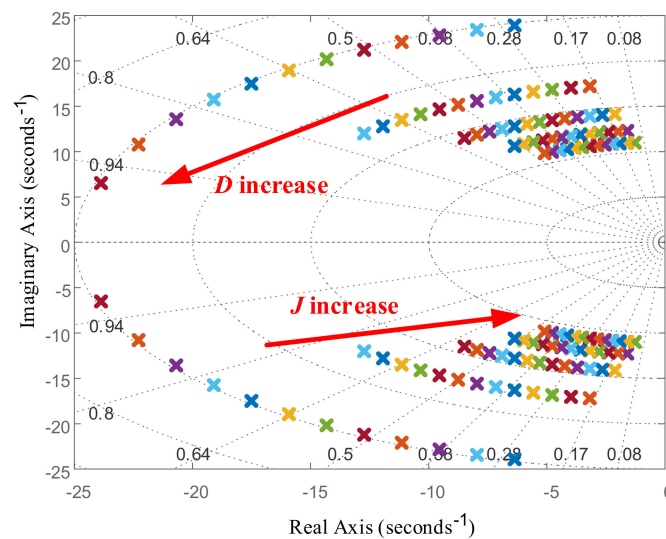
Figure 5. The changing trend of poles in GC mode.

In order to further investigate the effect of *J* and *D* on the active power response characteristics, the curve of P_{out} can be obtained when P_{set} steps 10 kW under different *J* and *D* in GC mode, as shown below.

In Figure 6, when *J* increases, the overshoot of P_{out} increases and the oscillation amplitude and settling time increase. When *D* increases, the overshoot of P_{out} decreases. This implies that a small *J* and a big *D* are beneficial to improve the power response transient characteristics and reduce the power overshoot and oscillation.

Similarly, the frequency response curve of ω_m can be obtained under different *J* and *D* when P_{set} steps 10 kW, as shown below.

In Figure 7, it can be seen that a large *J* helps to reduce ROCOF at the P_{set} step instant. during the subsequent process, a large *J* is beneficial to reduce the maximum frequency offset, but it increases the frequency oscillation time. Meanwhile, increasing *D* will reduce frequency oscillation.
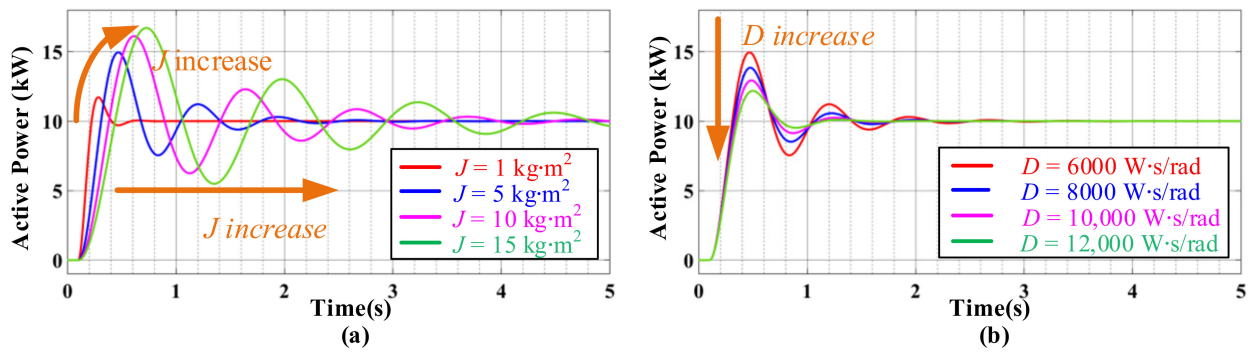
Figure 6. Power response curves under different *J* and *D*. (**a**) different *J* (**b**) different *D*.
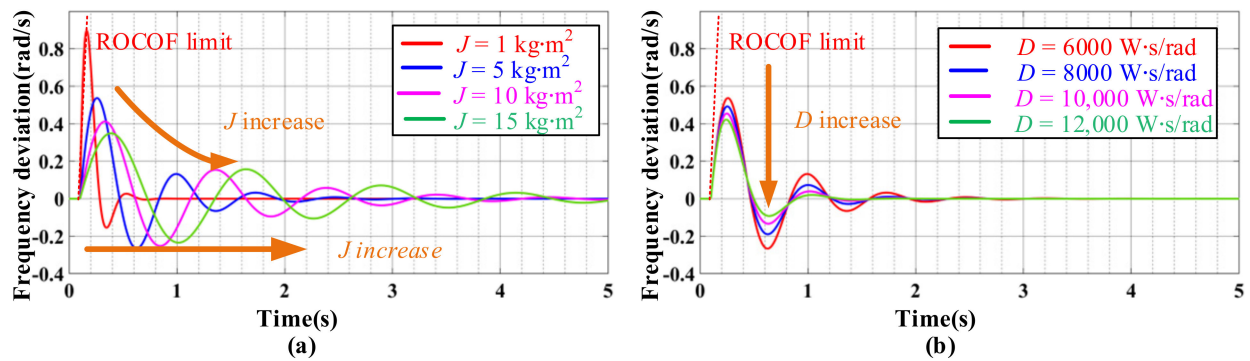
Figure 7. Frequency response curve under different *J* and *D*. (**a**) different *J* (**b**) different *D*.

Specifically, the ROCOF at the initial moment can be obtained from the initial theorem at the moment after the change of power reference command as:

$$\left.\frac{d\omega_m}{dt}\right|_{t=0} = \lim_{s\to\infty} s\cdot s\cdot \frac{\Delta\omega_m}{\Delta P_{set}}\cdot \frac{\Delta P_{set}}{s} = \frac{\Delta P_{set}}{J\omega_0} \tag{14}$$

This implies that a large *J* can reduce the ROCOF and can be beneficial to improve the frequency stability.

According to Figure 4, the closed-loop transfer function from ω_g to P_{out} in GC mode can be obtained as follows:

$$\left.\frac{\Delta P_{out}}{\Delta\omega_g}\right|_{GC} = -\frac{\frac{1}{s}\cdot\left(G_{\delta 2P} - \frac{G_{cq}\cdot G_{\delta 2Q}\cdot G_{E2P}}{1+G_{cq}\cdot G_{E2Q}}\right)}{1+G_{op1}} \tag{15}$$

According to Equation (15), the effect of ω_g on P_{out} in a steady state can be obtained as follows:

$$\Delta P_{out} = -\lim_{s\to 0} s\cdot \frac{\Delta\omega_g}{s}\cdot \frac{\frac{1}{s}\left(G_{\delta 2P} - \frac{G_{cq}\cdot G_{\delta 2Q}\cdot G_{E2P}}{1+G_{cq}\cdot G_{E2Q}}\right)}{1+G_{op1}} = -D\cdot\Delta\omega_g \tag{16}$$

Equation (16) shows that a large *D* can cause P_{out} to fluctuate sharply as ω_g fluctuates, and P_{out} may exceed its capacity limit, leading VSG to off-grid or shutdown.

In general, increasing the virtual inertia will increase the output power oscillation and reduce the frequency change rate of the system when VSG is operating and connected to the grid. Meanwhile, increasing the droop coefficient *D* will reduce power and frequency oscillation, but a large *D* can cause P_{out} to fluctuate sharply as ω_g fluctuates.

2.3. SA Mode

When CVSG operates in SA mode, the transfer function from P_{out} to ω_m can be obtained according to Equation (1) as follows:

$$\left.\frac{\Delta\omega_m}{\Delta P_{out}}\right|_{SA} = -\frac{1}{J\omega_0 s + D} \tag{17}$$

According to Equation (17), when CVSG operates in SA mode, the system behaves as a first-order system, and the only pole is:

$$s = -\frac{D}{J\omega_0} \tag{18}$$

Furthermore, the effect of different J and D on the frequency response curve in SA mode can be obtained as follows.

Figure 8 shows that in SA mode, a large J makes the frequency change smoother, and a large D makes the frequency deviation smaller in a steady state.
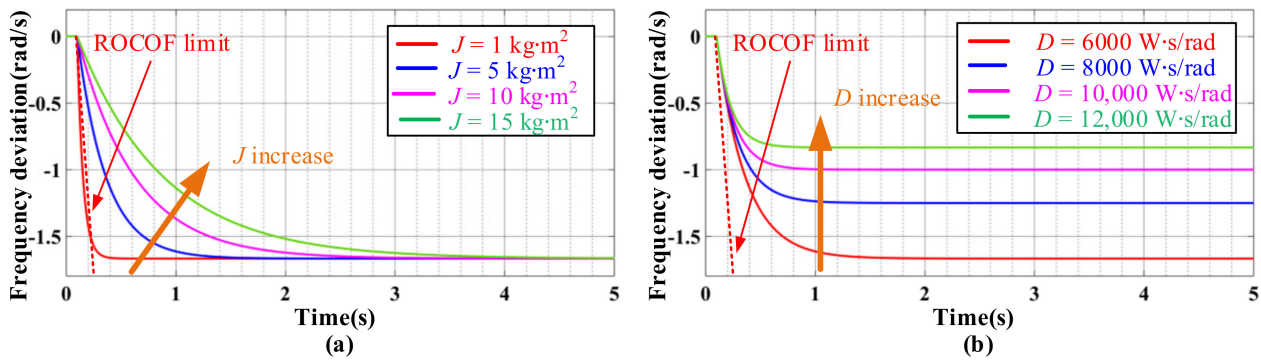
Figure 8. Frequency response curves under different J in SA mode. (**a**) different J (**b**) different D.

Specially, we can get that the ROCOF of CVSG at the P_{out} step instant as follows:

$$\left.\frac{d\omega_m}{dt}\right|_{t=0} = \lim_{s\to\infty} s\cdot s\cdot\frac{\Delta\omega_m}{\Delta P_{out}}\cdot\frac{\Delta P_{out}}{s} = \lim_{s\to\infty}\left(-s^2\frac{1}{J\omega_0 s + D}\frac{\Delta P_{out}}{s}\right) = -\frac{\Delta P_{out}}{J\omega_0} \tag{19}$$

The equation above shows that the ROCOF at the initial moment is strictly inversely proportional to the virtual inertia. Therefore, when VSG operates in SA mode, the larger the J, the better.

According to the final value theorem, when the system reaches a new steady state, the relationship of CVSG from P_{out} to ω_m can be obtained as follows:

$$\Delta\omega_m = -\lim_{s\to 0}\frac{1}{J\omega_0 s + D}\cdot s\cdot\frac{\Delta P_{out}}{s} = -\frac{\Delta P_{out}}{D} \tag{20}$$

The equation above shows that the frequency deviation in a steady state is strictly inversely proportional to the droop coefficient D.

In general, for CVSG, a large J can improve the frequency stability in both GC mode and SA mode, but can deteriorate the power response transient characteristics in GC mode. The droop coefficient D is directly related to the frequency deviation of the VSG and the steady-state power output, so its setting should be strictly in accordance with the rated power of the VSG.

3. VSG-EVI Control Strategy

As in the prior discussion of the tradeoff of virtual inertia, a large virtual inertia is needed to reduce ROCOF, but it also deteriorates the power and frequency oscillation

situations. This is actually the root cause for some other existing methods to suppress VSG oscillations to violate the ROCOF limits.

Therefore, the objective of our paper is to avoid the violation of the ROCOF limits when suppressing VSG oscillation. First, from the perspective of phase-frequency characteristics, a baseline is to be established to show how the phase margin is decreased due to increasing virtual inertia. Figure 9 shows the Bode diagram of the open-loop transfer function of the CVSG. As can be seen from the figure, the phase margin (PM) decreases continuously as J increases, which is responsible for the deteriorating dynamic performance of CVSG.
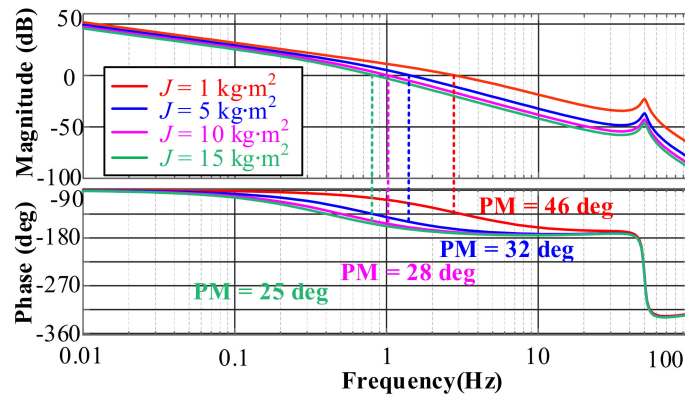
Figure 9. The Bode diagrams of the traditional VSG under different J.

Fortunately, different from the inertia of SG determined by the actual rotor, the inertia of the VSG can be adjusted freely; this is the essential advantage of VSG over SG, yet people only see part of this advantage, namely the ability to change the value of virtual inertia. In fact, we can not only change the value of virtual inertia, but also endow the virtual inertia with phase-frequency characteristics. This idea provides a new approach to improve the transient characteristics of CVSG. In this paper, the virtual inertia with phase-frequency characteristics is called extended virtual inertia (EVI), as follows:

$$J_1 = J \cdot \frac{s + k_1}{s + k_2} \tag{21}$$

Thus, the modified VSG is also called VSG-EVI, and the control block diagram of VSG-EVI can be obtained, as shown below Figure 10.
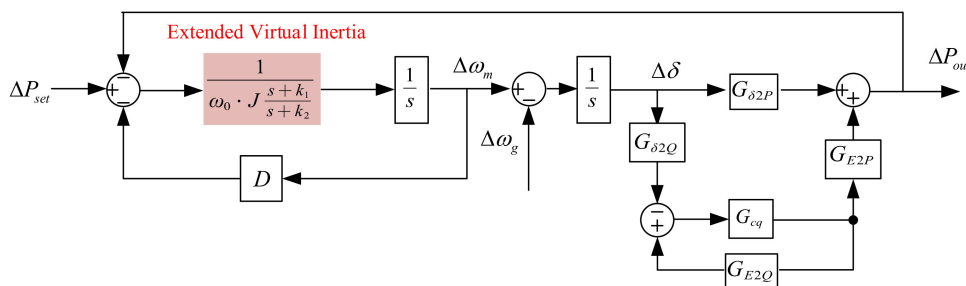
Figure 10. The control block diagram of VSG-EVI.

In Equation (21), VSG-EVI is equivalent to CVSG when $k_1 = k_2$. Therefore, CVSG can be considered as a special case of VSG-EVI. Further, we can draw the Bode diagram of CVSG with VSG-EVI.

As can be seen from Figure 11, the VSG-EVI improves the phase in the mid-band compared to the CVSG, thus increasing the phase margin of the whole system.
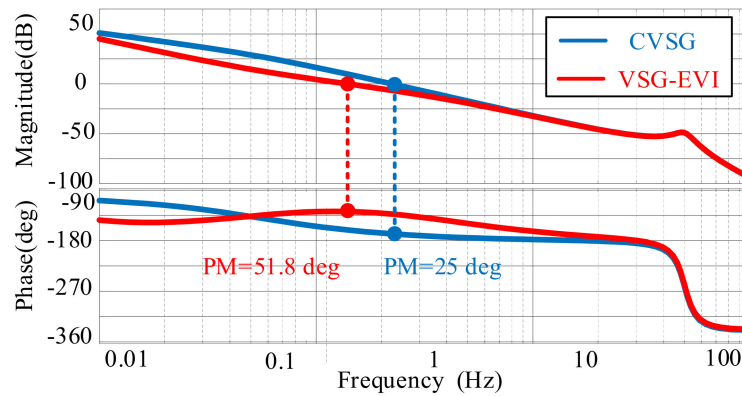
Figure 11. The Bode diagrams of the traditional VSG and VSG-EVI.

With the proposed extended virtual inertia, the VSG system transfer functions are then established subsequently under both GC and SA modes for detailed analysis and comparison with CVSG.

3.1. GC Mode

The active power loop gain of VSG-EVI can be obtained from Figure 8 as follows:

$$G_{OP1} = \frac{G_{cp1}}{s} \cdot \left(G_{\delta 2P} - \frac{G_{cq} \cdot G_{\delta 2Q} \cdot G_{E2P}}{1 - G_{cq} \cdot G_{E2Q}} \right) \tag{22}$$

where:

$$G_{cp1} = -\frac{s + k_2}{J\omega_0 s^2 + (J\omega_0 k_1 + D)s + k_2 D} \tag{23}$$

To investigate the effect of VSG-EVI on the power response in GC mode, the closed-loop transfer function from P_{set} to P_{out} of VSG-EVI can be obtained by combining Equations (22) and (23) as follows:

$$\frac{\Delta P_{out}}{\Delta P_{set}} = \frac{G_{OP1}}{1 + G_{OP1}} \tag{24}$$

From Equation (24), it can be obtained that the relationship between P_{set} and P_{out} at a steady state is as follows:

$$\Delta P_{out} = \lim_{s \to 0} s \cdot \frac{G_{OP1}}{1 + G_{OP1}} \cdot \frac{\Delta P_{set}}{s} = \Delta P_{set} \tag{25}$$

From Equation (25), it can be seen that VSG-EVI does not change the steady-state characteristics of the power response in GC mode.

To further investigate the effect of VSG-EVI on the frequency response in GC mode, the closed-loop transfer function from P_{set} to ω_m of VSG-EVI can be obtained by combining Equations (22) and (23) as follows:

$$\frac{\Delta \omega_m}{\Delta P_{set}} = \frac{G_{cp1}}{1 + G_{OP1}} \tag{26}$$

According to Equation (26), the ROCOF of VSG-EVI at the P_{set} step instant is as follows:

$$\left. \frac{d\omega_m}{dt} \right|_{t=0} = \lim_{s \to \infty} \frac{G_{cp1}}{1 + G_{OP1}} \cdot \frac{P_{set}}{s} \cdot s^2 = \frac{P_{set}}{J\omega_0} \tag{27}$$

Comparing Equations (14) and (27), it can be seen that CVSG and VSG-EVI have the same ROCOF at the P_{set} step instant for the same J, independent of k_1 and k_2. This implies that VSG-EVI does not change the maximum ROCOF, which is often considered to be an important feature of the frequency support characteristics of power systems.

In order to further investigate the effects of k_1 and k_2 on the active power response transient characteristics and frequency response transient characteristics, according to Equations (24) and (27), the P_{set} step response curves under different parameters are plotted in Figure 12. Figure 12a shows the power response curve, whereas Figure 12b shows the frequency response curve.
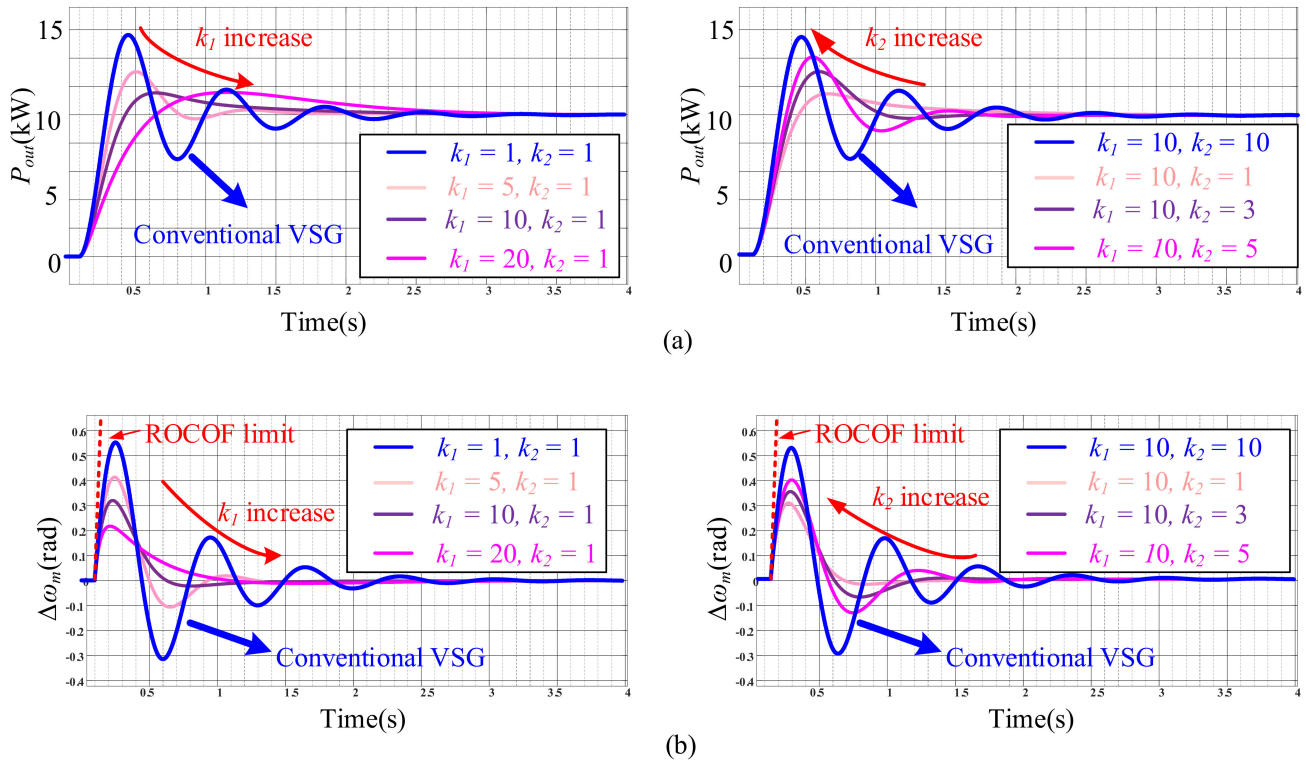
Figure 12. The frequency and power response curves of the system under different parameters: (**a**) power response curve, (**b**) frequency response curve.

For frequency, increasing k_1 or decreasing k_2 reduces the maximum offset of ω_m and reduces frequency oscillations. For power, increasing k_1 or decreasing k_2 suppresses power overshoot and power oscillation. Even under different k_1 and k_2, the initial (maximum) ROCOF is equal for all frequency response curves and the steady-state values are equal for all power response curves, which again proves that VSG-EVI does not change the frequency support characteristics and power control characteristics.

In general, in GC mode, VSG-EVI can improve the frequency response transient characteristics and power response transient characteristics without changing the frequency support characteristics and the steady-state characteristics of the power response.

3.2. SA Mode

The transfer function from P_{out} to ω_m for VSG-EVI in SA mode can be obtained from Figure 10 as follows:

$$\frac{\Delta\omega_m}{\Delta P_{out}} = -\frac{s + k_2}{J\omega_0 s^2 + (J\omega_0 k_1 + D)s + k_2 D} \tag{28}$$

According to Equation (28), the ROCOF of VSG-EVI at the P_{out} step instant can be obtained as follows:

$$\left.\frac{d\omega_m}{dt}\right|_{t=0} = -\lim_{s\to\infty}\frac{P_{out}}{s}s^2 \cdot \frac{s + k_2}{J\omega_0 s^2 + (J\omega_0 k_1 + D)s + k_2 D} = -\frac{P_{out}}{J\omega_0} \tag{29}$$

Comparing Equations (19) and (29), in SA mode, the maximum ROCOF of CVSG and VSG-EVI are equal, both related to the J, independent of k_1 and k_2. This implies that VSG-EVI does not change the frequency support characteristics in SA mode.

According to Equation (28), the time domain relationship of VSG-EVI from P_{out} to ω_m at a steady state can be obtained as follows:

$$\Delta\omega_m = -\lim_{s\to 0} s \cdot \frac{\Delta P_{out}}{s} \cdot \frac{s + k_2}{J\omega_0 s^2 + (J\omega_0 k_1 + D)s + k_2 D} = -\frac{\Delta P_{out}}{D} \tag{30}$$

Comparing Equations (20) and (30), the steady-state frequency deviations of both CVSG and VSG-EVI are determined by D in SA mode, independent of k_1 and k_2. This implies that VSG-EVI does not change the frequency-power droop characteristics in SA mode.

To further investigate the effect of k_1 and k_2 on the frequency response transient characteristics, based on Equation (28), the zero-pole distribution can be plotted (Figure 13).
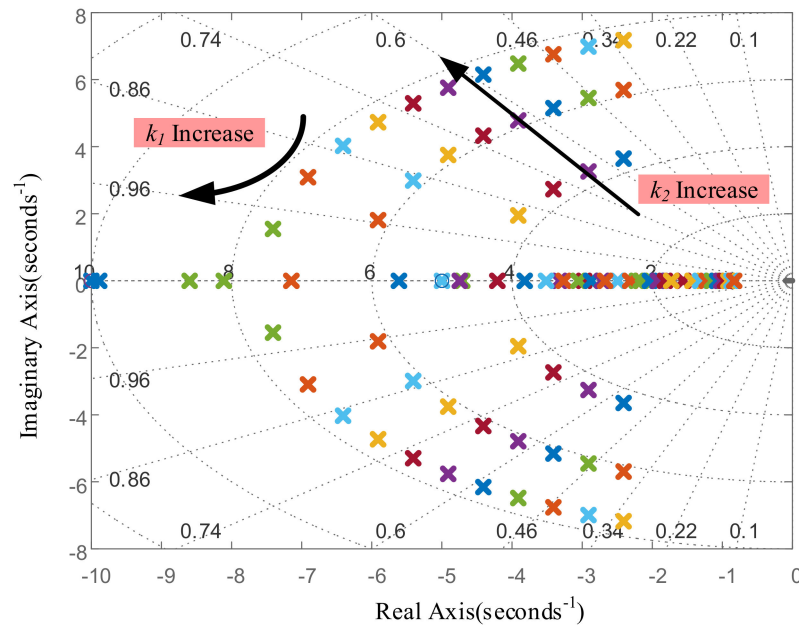
Figure 13. The zero-pole distribution of the system in SA mode.

As shown in Figure 13, when k_1 increases, the conjugate poles keep approaching the real axis. As k_1 continues to increase, the two conjugate poles turn into two real poles. When k_2 increases, the dominant pole shifts left and the damping ratio decreases. Note that in order to suppress frequency oscillations, the poles should be located on the real axis.

Correspondingly, we can also draw the frequency response curve in the variation of k_1 and k_2, as shown below.

As shown in Figure 14, when k_1 increases or k_2 decreases, the frequency of the system will become slower, but the ROCOF at the initial moment and frequency deviation in the steady state remain the same.

In summary, in both GC and SA mode, with reasonable parameters, VSG-EVI can improve frequency stability without changing the frequency-power droop characteristics and the maximum ROCOF.
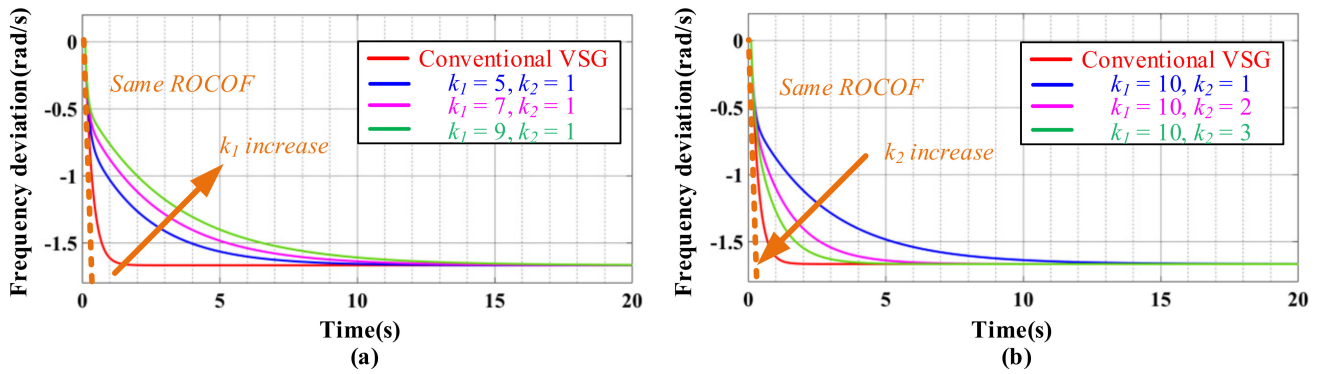
Figure 14. The frequency curves under different parameters in SA mode. (**a**) Effects of k_1, (**b**) effects of k_2.

4. Parameter Design

As the proposed VSG-EVI only manipulates the virtual inertia with frequency characteristics, the controller parameter design process is very straightforward and deterministic. No trial and error are needed, as seen in some existing papers.

4.1. Constraints for J and D

In GC mode, it can be seen from the above analysis that the ROCOF of the system is directly related to the value of the virtual inertia J, as follows:

$$\left.\frac{d\omega_m}{dt}\right|_{t=0} = \frac{\Delta P_{set}}{J\omega_0} \tag{31}$$

Assuming that the maximum ROCOF limit is λ Hz/s, taking into account an extreme case where the reference power increases abruptly from 0 to the rated value, the virtual inertia should satisfy, and J should satisfy the following constraint:

$$J \geqslant \frac{\Delta P_{set}}{2\pi f_0 \lambda} \tag{32}$$

The effect of ω_g on P_{out} in a steady state is as follows:

$$\Delta P_{out} = -D \cdot \Delta\omega_g \tag{33}$$

So, the value of D cannot be too large.

In SA mode, at the P_{out} step instant, the ROCOF of the system is directly related to the value of the virtual inertia J, as follows:

$$\left.\frac{d\omega_m}{dt}\right|_{t=0} = -\frac{\Delta P_{out}}{J\omega_0} \tag{34}$$

Assuming that the maximum ROCOF limit is λ Hz/s, J should satisfy the following constraint:

$$J \geqslant \frac{\Delta P_{out}}{2\pi f_0 \lambda} \tag{35}$$

This is the same requirement for virtual inertia in GC mode.

In a steady state, the time domain relationship from P_{out} to ω_m of VSG-EVI is repeated as follows:

$$\Delta\omega_m = -\frac{\Delta P_{out}}{D} \tag{36}$$

Assuming that the maximum frequency deviation limit is $\Delta f_{\max}$ Hz, D should satisfy the following constraint:

$$D \geqslant \frac{P_{out}}{2\pi \cdot \Delta f_{\max}} \tag{37}$$

From the previous analysis, it is concluded that in GC mode, a large J is beneficial to reduce the maximum ROCOF and improve frequency stability. However, a large J will reduce the PM of the active power control loop and seriously deteriorate the active power response transient characteristics. Therefore, considering the limitations in the GC and SA modes together, it is sufficient to choose slightly larger than the minimum J determined by Equation (35).

According to Equation (37), D is also limited by the capacity and the maximum frequency offset in SA mode. Therefore, considering the limitations of SA and GC modes together, it is sufficient to choose slightly larger than the minimum D which is determined by Equation (36).

4.2. Design of EVI Parameters

Compared with the power controller G_{cp} of CVSG, the power controller G_{cp1} of the VSG-EVI replaces the pole of $s = -D/J\omega_0$ in CVSG with one zero and two poles. The zero point and the two poles are shown below:

$$z_0 = -k_2 \tag{38}$$

$$p_{1,2} = \frac{-(J\omega_0 k_1 + D)}{2J\omega_0} \pm \frac{\sqrt{(J\omega_0 k_1 + D)^2 - 4J\omega_0 D k_2}}{2J\omega_0} \tag{39}$$

The zero is determined by k_2 as shown in Equation (33). In order to improve PM, the amplitude-frequency curve of the active power control loop should be made to cross 0 dB with a slope of -20 dB/dec. Therefore, the new added zero should be made to fall before the cut-off frequency ω_c of the active power control loop gain of CVSG, and a certain distance should be kept. Thus, the constraints of k_2 can be obtained as follows:

$$k_2 \ll \omega_c \tag{40}$$

where:

$$20\lg\left| \frac{G_{cp}}{s} \cdot \left(G_{\delta 2P} - \frac{G_{cq} \cdot G_{\delta 2Q} \cdot G_{E2P}}{1 - G_{cq} \cdot G_{E2Q}} \right) \right|_{s=j\omega_c} = 0 \tag{41}$$

In the SA mode, in order to eliminate frequency oscillation (or make system work in overdamped state), the poles should be placed on the real axis. Therefore, k_1 and k_2 should satisfy:

$$\xi = \frac{k_1 J\omega_0 + D}{2\sqrt{k_2 J\omega_0 D}} \geqslant 1 \tag{42}$$

The constraints of k_1 can be obtained by combining Equations (30) and (35) as follows:

$$k_1 \geqslant \frac{(1 - 2\sqrt{k_2 J\omega_0 D}) - D}{J\omega_0} \tag{43}$$

4.3. Parameter Design Flow

When all parameters are selected, it can be judged according to Equation (17) whether the PM and cut-off frequency of the active power control loop gain of VSG-EVI can meet the requirements. If the design requirements cannot be met, it is necessary to return to Equation (16) and redesign k_2. The complete parameter design flow is shown in Figure 15.
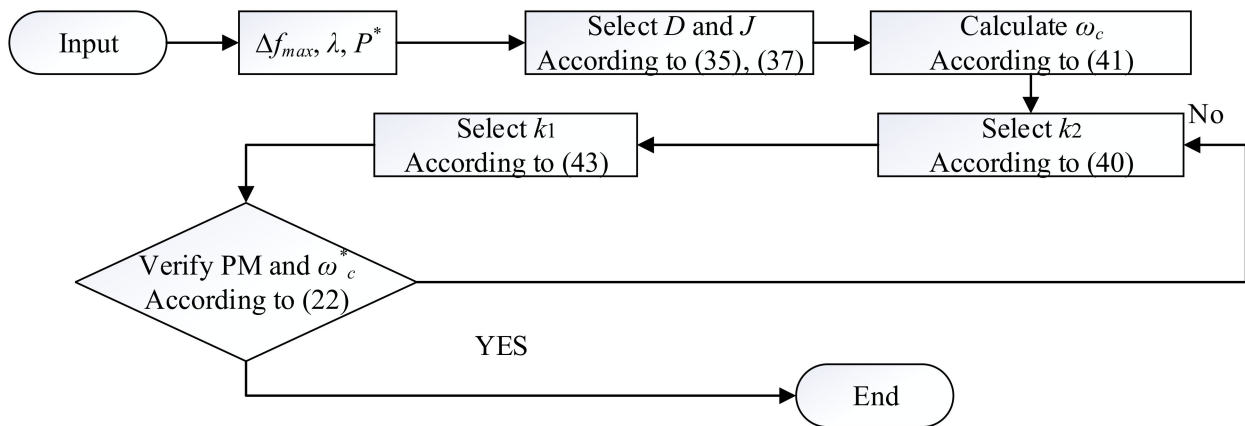
Figure 15. Parameter design flow.

In this paper, the circuit parameters and the main control parameters are shown in Table 1.

Table 1. Circuit Parameters.

Parameter	Value	Parameter	Value
V_g	220 V	C	30 uF
V_{dc}	700 V	L_2	1500 uH
f_0	50 Hz	D	6000
S^*	10 kVA	J	5.5
f_{sw}	20 kHz	k_1	10
L_1	400 uH	k_2	1

5. Experimental Verifications

In order to verify the effectiveness of the VSG-EVI proposed in this paper, three-phase VSG prototypes were tested in our microgrid testbed, with the detailed circuit parameters and control parameters shown in Table 1. In the experiments, a real-time supervisory control console is used to control VSG and acquire the data sent from DSP via the CAN bus. Our complete microgrid testbed is shown in Figure 16.

Figure 16. Experimental platform.

5.1. SA Mode

The purpose of this subsection is to experimentally validate the difference in frequency response between CVSG and VSG-EVI in SA mode, and the effect of k_1 and k_2 on the frequency response. In the experiment, the prototype is running unloaded first, and then a

10 kW load is inserted. After the output frequency of the prototype is stable, the load is removed. During the whole experiment, the output frequency is recorded through the CAN bus in main control computer, and the output voltage and output current are recorded through an oscilloscope. The output current is mainly determined by the load, so the envelopes of the output voltage and output current for these four cases are approximately the same with the same load, as shown in Figure 17.
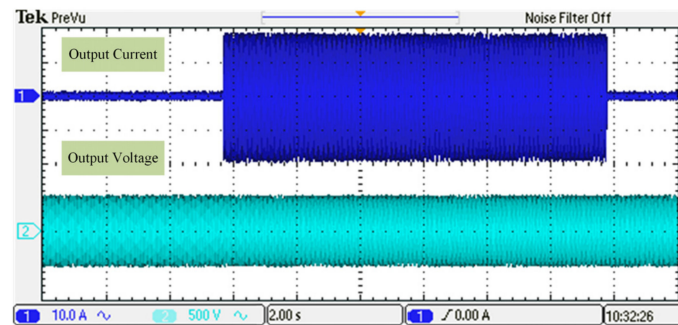
Figure 17. Experimental results of voltage and current in SA mode.

Figure 18 shows the frequency curve. Figure 18a shows the experimental results of conventional VSG and Figure 18b–d shows the experimental results of VSG-EVI with different parameters.
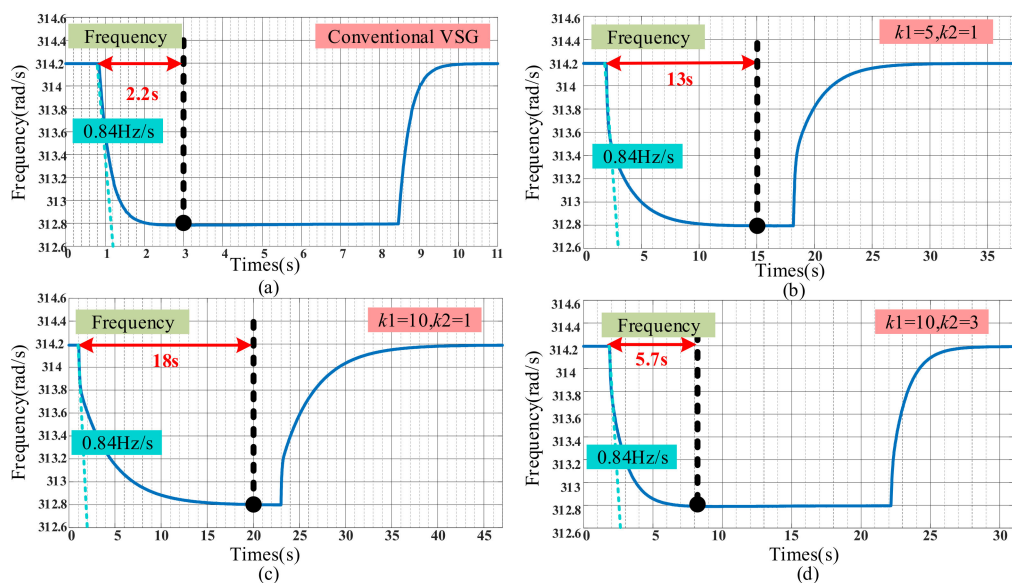
Figure 18. Experimental results of frequency in SA mode (**a**) conventional VSG (**b**) $k_1 = 5$, $k_2 = 1$ (**c**) $k_1 = 10$, $k_2 = 1$ (**d**) $k_1 = 10$, $k_2 = 3$.

Comparing Figure 18a–d, it can be seen that VSG-EVI does not change the maximum ROCOF at the load step instant and the frequency deviation in a steady state compared to conventional VSG. This implies that VSG-EVI does not change the frequency support characteristics and frequency-power droop characteristics in SA mode. Note that the VSG-EVI has a smoother frequency curve, which improves frequency stability.

By comparing Figure 18b,c, it can be seen that when k_1 increases, the frequency response speed decreases. Similarly, comparing Figure 18c,d, it can be seen that the frequency response speed increases when k_2 increases.

5.2. GC Mode

The purpose of this subsection is to experimentally validate the power command tracking abilities of VSG-EVI and to compare the active power response transient characteristics of CVSG and VSG-EVI. In the experiment, the prototype is first pre-synchronized with the grid and then connects into the grid. The main control computer sends a 10 kW step power command, and after the output active power is stable, the power command steps to 0 kW. During the whole experiment, the output active power is recorded through the CAN bus in the main control computer, and the output current is recorded through an oscilloscope. In Figure 19, the left graph is the output active power curve and the right graph is the output current curve. Figure 19a shows the experimental results of conventional VSG, and Figure 19b–d shows the experimental results of VSG-EVI with different parameters.
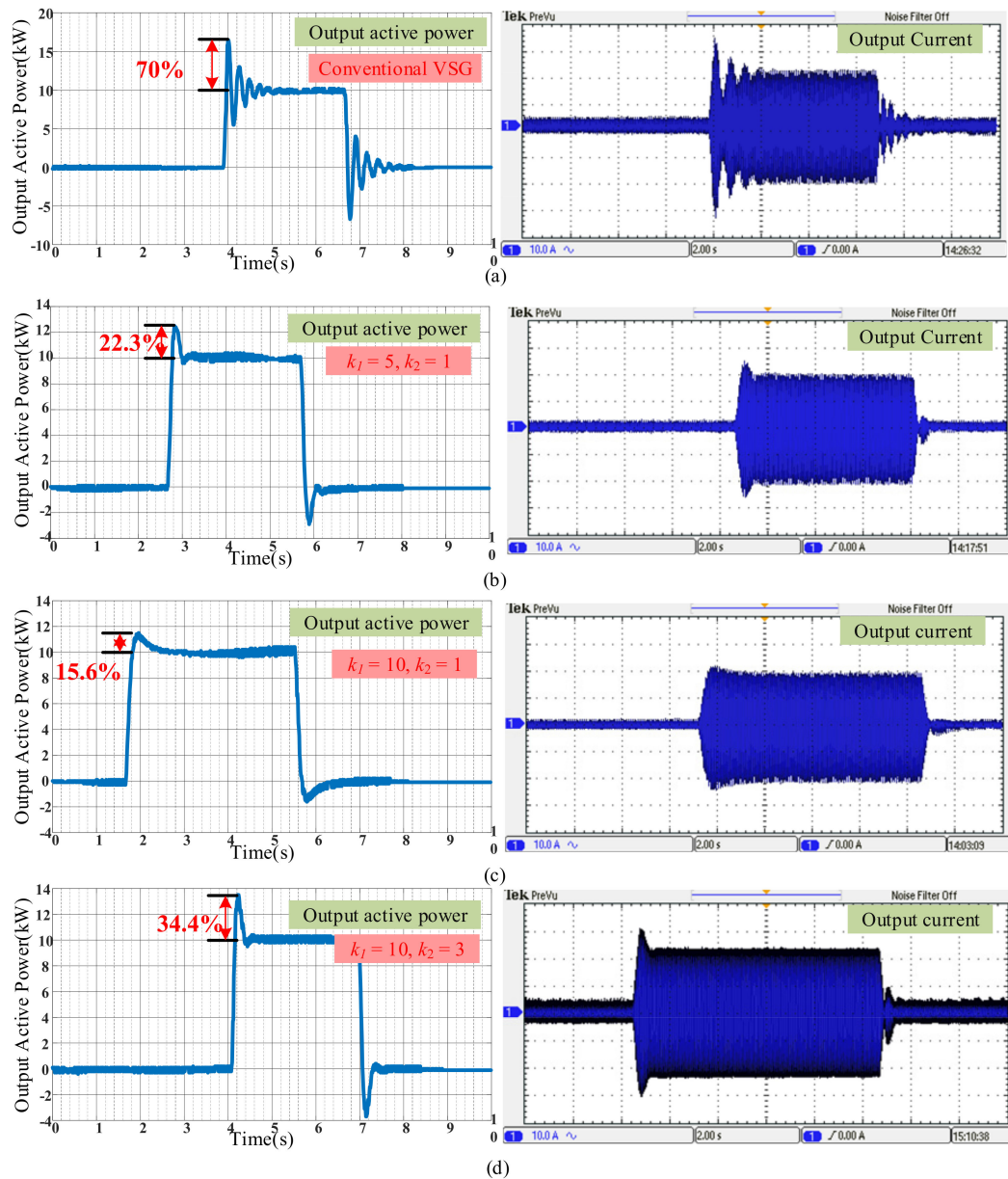
Figure 19. Experimental results in GC mode: (**a**) conventional VSG; (**b**) $k_1 = 5$, $k_2 = 1$; (**c**) $k_1 = 10$, $k_2 = 1$; (**d**) $k_1 = 10$, $k_2 = 3$.

In Figure 19a, the output active power of CVSG shows an overshoot up to 70% with large oscillations when the active power command steps. This implies that power

electronics have to bear current inrush that far exceeds their capacity. Compared to the CVSG in Figure 19a, VSG-EVI in Figure 19b–d significantly reduces the output active power overshoot, eliminates power oscillations, and greatly improves the active power response transient characteristics. In a steady state, VSG-EVI tracks the active power command just as well as the CVSG.

Comparing Figure 19b,c, it can be seen that the overshoot of the active power response decreases when k_1 increases. Comparing Figure 19c,d, it can be seen that the response speed increases when k_2 increases, whereas the overshoot of the active power response increases. The experimental results coincide with the theoretical results in Figure 12.

6. Conclusions

To suppress VSG power and frequency oscillation, many existing methods have been proposed so far. Though they are effective at suppressing the VSG oscillation, they suffer from issues such as the reduction of frequency support capability and a complex controller tuning process. This paper proposes a universal VSG control strategy based on extended virtual inertia (VSG-EVI) to addresses these issues while retaining the effectiveness of VSG oscillation suppression. As EVI, the virtual inertia is no longer a constant or varying number; it is endowed with frequency domain characteristics to improve the VSG transient responses. Meanwhile, the controller parametric design process is also very much simplified with the proposed intuitive extended virtual inertia, and comprehensive design constraints and a design flow considering both GC and SA modes are introduced.

The VSG-EVI lab prototype experiments were thoroughly performed in our microgrid testbed. Compared with the CVSG lab results, the proposed VSG-EVI increases the system phase margin from 25° to 51.8°, and significantly reduces the 70% active power overshoot to 15.6%. Compared to some other VSG oscillation suppression methods that violate the ROCOF limits, VSG-EVI maintains a stable initial ROCOF at 0.84 Hz/s in SA mode and GC mode, indicating that the VSG-EVI does not reduce the inertia support capability in either SA mode or GC mode.

It should be mentioned that even though VSG-EVI is proposed with a single VSG under both GC and SA modes, this method can be extended to multiple VSG parallel application scenarios in future studies.

Nomenclature

J	Virtual inertia
D	Droop coefficient of active power control
D_q	Droop coefficient of reactive power control
K	Virtual excitation regulation coefficient
P_{set}, Q_{set}	Command of power
P_{out}, Q_{out}	Output power
ω_m, ω_{ref}	Output frequency and reference frequency
U_{out}, U_{ref}	Amplitude of voltage and reference voltage
L_g	The total equivalent line inductance
R_g	The total equivalent line resistance

X_g	The total equivalent line reactance
Δx	Small signal of x
$G_{\delta 2P}$, G_{E2P}, G_{U2P}	Transfer function of active power
$G_{\delta 2Q}$, G_{E2Q}, G_{U2Q}	Transfer function of reactive power
G_{cp}, G_{cp1}, G_{cq}	Controller
G_{op}, G_{op1}	Loop gain of active power control
k_1, k_2	Parameter of VSG-EVI
ω_c	Cut-off frequency

References

1. Mansouri, S.A.; Ahmarinejad, A.; Sheidaei, F.; Javadi, M.S.; Rezaee Jordehi, A.; Esmaeel Nezhad, A.; Catalão, J.P.S. A Multi-Stage Joint Planning and Operation Model for Energy Hubs Considering Integrated Demand Response Programs. *Int. J. Electr. Power Energy Syst.* **2022**, *140*, 108103. [CrossRef]
2. Mansouri, S.A.; Rezaee Jordehi, A.; Marzband, M.; Tostado-Véliz, M.; Jurado, F.; Aguado, J.A. An IoT-Enabled Hierarchical Decentralized Framework for Multi-Energy Microgrids Market Management in the Presence of Smart Prosumers Using a Deep Learning-Based Forecaster. *Appl. Energy* **2023**, *333*, 120560. [CrossRef]
3. Mansouri, S.; Ahmarinejad, A.; Javadi, M.; Esmaeel Nezhad, A.; Shafie-khah, M.; Catalão, J. Demand Response Role for Enhancing the Flexibility of Local Energy Systems. In *Distributed Energy Resources in Local Integrated Energy Systems*; Elsevier: Amsterdam, The Netherlands, 2021; pp. 279–313. ISBN 978-0-12-823899-8.
4. Mansouri, S.A.; Ahmarinejad, A.; Nematbakhsh, E.; Javadi, M.S.; Jordehi, A.R.; Catalao, J.P.S. Energy Hub Design in the Presence of P2G System Considering the Variable Efficiencies of Gas-Fired Converters. In Proceedings of the 2021 International Conference on Smart Energy Systems and Technologies (SEST), Vaasa, Finland, 6–8 September 2021; pp. 1–6.
5. Hosseini, S.E.; Ahmarinejad, A.; Tabrizian, M.; Bidgoli, M.A. Resilience Enhancement of Integrated Electricity-Gas-Heating Networks through Automatic Switching in the Presence of Energy Storage Systems. *J. Energy Storage* **2022**, *47*, 103662. [CrossRef]
6. Barik, A.K.; Das, D.C. Integrated Resource Planning in Sustainable Energy-Based Distributed Microgrids. *Sustain. Energy Technol. Assess.* **2021**, *48*, 101622. [CrossRef]
7. Bhuyan, M.; Das, D.C.; Barik, A.K. Proficient Power Control Strategy for Combined Solar Gas Turbine-wind Turbine Generator-biodiesel Generator Based Two Area Interconnected Microgrid Employed with DC Link Using Harris's Hawk Optimization Optimised Tilt-integral-derivative Controller. *Int. J. Numer. Model.* **2022**, *35*, e2991. [CrossRef]
8. Barakat, M.; Donkol, A.; Hamed, H.F.A.; Salama, G.M. Harris Hawks-Based Optimization Algorithm for Automatic LFC of the Interconnected Power System Using PD-PI Cascade Control. *J. Electr. Eng. Technol.* **2021**, *16*, 1845–1865. [CrossRef]
9. Barik, A.K.; Das, D.C.; Latif, A.; Hussain, S.M.S.; Ustun, T.S. Optimal Voltage–Frequency Regulation in Distributed Sustainable Energy-Based Hybrid Microgrids with Integrated Resource Planning. *Energies* **2021**, *14*, 2735. [CrossRef]
10. Guerrero, J.M.; Vasquez, J.C.; Matas, J.; de Vicuna, L.G.; Castilla, M. Hierarchical Control of Droop-Controlled AC and DC Microgrids—A General Approach Toward Standardization. *IEEE Trans. Ind. Electron.* **2011**, *58*, 158–172. [CrossRef]
11. Rocabert, J.; Luna, A.; Blaabjerg, F.; Rodríguez, P. Control of Power Converters in AC Microgrids. *IEEE Trans. Power Electron.* **2012**, *27*, 4734–4749. [CrossRef]
12. Wang, Z.; Chen, B.; Wang, J.; Kim, J. Decentralized Energy Management System for Networked Microgrids in Grid-Connected and Islanded Modes. *IEEE Trans. Smart Grid* **2016**, *7*, 1097–1105. [CrossRef]
13. Ratnam, K.S.; Palanisamy, K.; Yang, G. Future Low-Inertia Power Systems: Requirements, Issues, and Solutions—A Review. *Renew. Sustain. Energy Rev.* **2020**, *124*, 109773. [CrossRef]
14. Fang, J.; Li, H.; Tang, Y.; Blaabjerg, F. On the Inertia of Future More-Electronics Power Systems. *IEEE J. Emerg. Sel. Top. Power Electron.* **2019**, *7*, 2130–2146. [CrossRef]
15. Shazon, M.N.H.; Nahid-Al-Masood; Ahmed, H.M.; Deeba, S.R.; Hossain, E. Exploring the Utilization of Energy Storage Systems for Frequency Response Adequacy of a Low Inertia Power Grid. *IEEE Access* **2021**, *9*, 129933–129950. [CrossRef]
16. Abuagreb, M.; Allehyani, M.F.; Johnson, B.K. Overview of Virtual Synchronous Generators: Existing Projects, Challenges, and Future Trends. *Electronics* **2022**, *11*, 2843. [CrossRef]
17. Vorwerk, J.; Markovic, U.; Hug, G. Comparing the Damping Capabilities of Different Fast-Frequency Controlled Demand Technologies. In Proceedings of the 2021 IEEE Madrid PowerTech, Madrid, Spain, 28 June–2 July 2021; pp. 1–6.
18. Shin, H.; Hur, J. Optimal Energy Storage Sizing with Battery Augmentation for Renewable-Plus-Storage Power Plants. *IEEE Access* **2020**, *8*, 187730–187743. [CrossRef]
19. Allehyani, M.F.; Abuagreb, M.; Johnson, B.K. The Effect of Frequency Droop Damping on System Parameters and Battery Sizing During Load Change Condition. In Proceedings of the 2022 International Conference on Electrical, Computer and Energy Technologies (ICECET), Prague, Czech Republic, 20–22 July 2022; pp. 1–5.
20. Abuagreb, M.; Ajao, B.; Herbert, H.; Johnson, B.K. Evaluation of Virtual Synchronous Generator Compared to Synchronous Generator. In Proceedings of the 2020 IEEE Power & Energy Society Innovative Smart Grid Technologies Conference (ISGT), Washington, DC, USA, 17–20 February 2020; pp. 1–5.
21. Driesen, J.; Visscher, K. Virtual Synchronous Generators. In Proceedings of the 2008 IEEE Power and Energy Society General Meeting—Conversion and Delivery of Electrical Energy in the 21st Century, Pittsburgh, PA, USA, 20–24 July 2008; pp. 1–3.

22. Duan, Q.; Zhao, C. Improved VSG Controlled SST in a Low-Voltage AC Distribution Network. In Proceedings of the 2021 IEEE Sustainable Power and Energy Conference (iSPEC), Nanjing, China, 23–25 December 2021; pp. 428–435.

23. Wu, H.; Ruan, X.; Yang, D.; Chen, X.; Zhao, W.; Lv, Z.; Zhong, Q. Small-Signal Modeling and Parameters Design for Virtual Synchronous Generators. *IEEE Trans. Ind. Electron.* **2016**, *63*, 4292–4303. [CrossRef]

24. Mercier, P.; Cherkaoui, R.; Oudalov, A. Optimizing a Battery Energy Storage System for Frequency Control Application in an Isolated Power System. *IEEE Trans. Power Syst.* **2009**, *24*, 1469–1477. [CrossRef]

25. Zhang, Y.J.A.; Zhao, C.; Tang, W.; Low, S.H. Profit-Maximizing Planning and Control of Battery Energy Storage Systems for Primary Frequency Control. *IEEE Trans. Smart Grid* **2018**, *9*, 712–723. [CrossRef]

26. Shang, L.; Dong, X.; Liu, C.; Gong, Z. Fast Grid Frequency and Voltage Control of Battery Energy Storage System Based on the Amplitude-Phase-Locked-Loop. *IEEE Trans. Smart Grid* **2022**, *13*, 941–953. [CrossRef]

27. Alipoor, J.; Miura, Y.; Ise, T. Stability Assessment and Optimization Methods for Microgrid with Multiple VSG Units. *IEEE Trans. Smart Grid* **2018**, *9*, 1462–1471. [CrossRef]

28. Hou, X.; Han, H.; Zhong, C.; Yuan, W.; Yi, M.; Chen, Y. Improvement of Transient Stability in Inverter-Based AC Microgrid via Adaptive Virtual Inertia. In Proceedings of the 2016 IEEE Energy Conversion Congress and Exposition (ECCE), Milwaukee, WI, USA, 18–22 September 2016; pp. 1–6.

29. Qu, S.; Wang, Z. Cooperative Control Strategy of Virtual Synchronous Generator Based on Optimal Damping Ratio. *IEEE Access* **2021**, *9*, 709–719. [CrossRef]

30. Li, J.; Wen, B.; Wang, H. Adaptive Virtual Inertia Control Strategy of VSG for Micro-Grid Based on Improved Bang-Bang Control Strategy. *IEEE Access* **2019**, *7*, 39509–39514. [CrossRef]

31. Ren, M.; Li, T.; Shi, K.; Xu, P.; Sun, Y. Coordinated Control Strategy of Virtual Synchronous Generator Based on Adaptive Moment of Inertia and Virtual Impedance. *IEEE J. Emerg. Sel. Top. Circuits Syst.* **2021**, *11*, 99–110. [CrossRef]

32. Yang, Y.; Xu, J.; Li, C.; Zhang, W.; Wu, Q.; Wen, M.; Blaabjerg, F. A New Virtual Inductance Control Method for Frequency Stabilization of Grid-Forming Virtual Synchronous Generators. *IEEE Trans. Ind. Electron.* **2023**, *70*, 441–451. [CrossRef]

33. Meng, X.; Liu, J.; Liu, Z. A Generalized Droop Control for Grid-Supporting Inverter Based on Comparison between Traditional Droop Control and Virtual Synchronous Generator Control. *IEEE Trans. Power Electron.* **2019**, *34*, 5416–5438. [CrossRef]

34. Li, M.; Yu, P.; Hu, W.; Wang, Y.; Shu, S.; Zhang, Z.; Blaabjerg, F. Phase Feedforward Damping Control Method for Virtual Synchronous Generators. *IEEE Trans. Power Electron.* **2022**, *37*, 9790–9806. [CrossRef]

35. Gao, C.; Liu, X.; Chen, H. Research on the Control Strategy of Distributed Energy Resources Inverter Based on Improved Virtual Synchronous Generator. *Sci. Rep.* **2017**, *7*, 9025. [CrossRef] [PubMed]